

# Experimental investigation of immersed granular collapse in viscous and inertial regimes

Cite as: Phys. Fluids **33**, 103317 (2021); <https://doi.org/10.1063/5.0067485>

Submitted: 17 August 2021 • Accepted: 28 September 2021 • Published Online: 15 October 2021

Yunhui Sun (孙云辉), Wentao Zhang (张炆涛),  Yi An (安翼), et al.

## COLLECTIONS

 This paper was selected as an Editor's Pick



View Online



Export Citation



CrossMark

## ARTICLES YOU MAY BE INTERESTED IN

[An experimental study on aquatic collapses of bidisperse granular deposits](#)

Physics of Fluids **33**, 103311 (2021); <https://doi.org/10.1063/5.0065346>

[Numerical study on immersed granular collapse in viscous regime by particle-scale simulation](#)

Physics of Fluids **32**, 073313 (2020); <https://doi.org/10.1063/5.0015110>

[Robust deep learning for emulating turbulent viscosities](#)

Physics of Fluids **33**, 105118 (2021); <https://doi.org/10.1063/5.0064458>

APL Machine Learning

Open, quality research for the networking communities

**Now Open for Submissions**

LEARN MORE



# Experimental investigation of immersed granular collapse in viscous and inertial regimes

Cite as: Phys. Fluids **33**, 103317 (2021); doi: [10.1063/5.0067485](https://doi.org/10.1063/5.0067485)

Submitted: 17 August 2021 · Accepted: 28 September 2021 ·

Published Online: 15 October 2021





View Online



Export Citation



CrossMark

Yunhui Sun (孙云辉),<sup>1</sup> Wentao Zhang (张焱涛),<sup>2,3</sup> Yi An (安翼),<sup>2</sup>  Qingquan Liu (刘青泉),<sup>1,a)</sup>   
and Xiaoliang Wang (王晓亮)<sup>1,a)</sup>

## AFFILIATIONS

<sup>1</sup>School of Aerospace Engineering, Beijing Institute of Technology, Beijing 100081, China

<sup>2</sup>Key Laboratory for Mechanics in Fluid Solid Coupling Systems, Institute of Mechanics, Chinese Academy of Sciences, Beijing 100190, China

<sup>3</sup>Midea Corporate Research Center, Foshan 528311, Guangdong, China

<sup>a)</sup>Authors to whom correspondence should be addressed: [liuqq@bit.edu.cn](mailto:liuqq@bit.edu.cn) and [wangxiaoliang36@bit.edu.cn](mailto:wangxiaoliang36@bit.edu.cn)

## ABSTRACT

This paper presents an experimental investigation of immersed granular collapse with an initially dense packing, mainly focusing on the collapse characteristics of different flow regimes and the influence of the initial aspect ratio. A novel experimental setup and imaging method are introduced to simultaneously observe the motion of the particles and the fluid. The collapse dynamics, including the collapse acceleration, steady propagation velocity, and collapse duration, are analyzed based on the front propagation. It is found that the collapse procedures in the inertial and viscous regimes differ significantly, with the transitional regime possessing some unique characteristics of both. The inertial regime exhibits a faster collapse process, sharper final deposition, and a depression near the right wall in the case of high columns. The viscous regime collapses from the upper-left corner, from where particles drop to the bottom and form the flow front in advance of the particles initially at the bottom, and exhibits a triangular final deposition. The inertial regime exhibits swirling fluid motion, which helps the granular transport, whereas the fluid flow in the viscous regime mainly follows the granular flow. The collapse regime characteristics are more pronounced in higher columns.

Published under an exclusive license by AIP Publishing. <https://doi.org/10.1063/5.0067485>

## I. INTRODUCTION

Particle–fluid mixture flows are common in natural events such as debris flows, landslides, and turbidity currents. The existence of the fluid dramatically changes the granular flow because of the complex particle–fluid interactions. For example, submarine landslides can happen on very shallow inclinations ( $<1^\circ$ ) and may travel several orders of magnitude farther than their terrestrial counterparts.<sup>1</sup> Submarine landslides are also more destructive, generating tsunamis, and damaging offshore infrastructure.<sup>2</sup> As a simplified model of natural granular flows, small-scale granular collapse has been widely studied for its rich dynamics and simple configuration. In this unsteady problem, an initially static granular column collapses onto the horizontal plane under gravity. Depending on the properties of both the particles and the fluid, the collapse may be assigned to different flow regimes,<sup>3,4</sup> each having particular collapse features. Basically, the flow regime is defined based on the moving characteristics of the particles. For a single particle dropping in fluid, the main driving force is gravity  $g$  and the resistance is the drag force. Along the direction of the gravity,

assuming the flow being stationary, the motion of the particle is governed by

$$\frac{\pi}{6}d^3\rho_p\frac{dv_p}{dt} = \frac{\pi}{6}d^3(\rho_p - \rho_f)g - F_d. \quad (1)$$

Here,  $d$  is the particle diameter,  $v_p$  is the particle velocity, and  $\rho_p$  ( $\rho_f$ ) is the particle (fluid) density and  $\rho_p > \rho_f$ .  $F_d$  is the drag force applied on a single particle, expressed by<sup>5</sup>

$$F_d = C_d \frac{\pi d^2 \rho_f v_p^2}{4}. \quad (2)$$

Note that in terms of the hydrodynamic force, only the drag force is considered since it is the most significant.<sup>6</sup> The drag force coefficient  $C_d$  depends on the particle Reynolds number  $Re_p = \rho_f v_p d / \mu_f$ , where  $\mu_f$  is the dynamic viscosity of the fluid. A comprehensive review of the expressions of  $C_d$  is given by Goossens.<sup>5</sup> In a perfectly laminar flow or viscous regime ( $Re_p < 0.5$ ),  $C_d = 24/Re_p$ , whereas in a turbulent flow or inertial regime ( $Re_p > 1000$ ),  $C_d$  remains almost constant at around

0.4. By solving Eq. (1) analytically, timescales of  $\tau_I$  and  $\tau_V$  are obtained for the inertial and viscous regimes, respectively. In addition, for a particle moving in the air, for which the drag force is negligible, we can define the time required for the particle to move one particle diameter as the free fall timescale  $\tau_{FF}$  (see the detailed solving procedure and expressions of the timescales in Pont *et al.*<sup>3</sup> and Jing *et al.*<sup>7</sup>). Then, two dimensionless numbers are defined:

$$St = \frac{\tau_V}{\tau_{FF}} = \frac{1}{18\mu_f} \sqrt{\frac{\rho_p(\rho_p - \rho_f)gd^3}{2}}, \quad r = \frac{\tau_I}{\tau_{FF}} = \sqrt{\frac{\rho_p}{\rho_f}}, \quad (3)$$

which compare the three timescales to evaluate the relative importance of the inertial regime, viscous regime, and free fall regime. As shown in previous investigations,<sup>3,4</sup> the Stokes number  $St$  and density ratio  $r$  determine the granular flow regime, and a phase diagram can be determined, as shown in Fig. 1. Dry granular collapse, that is, collapse in the air where the ambient fluid can be ignored, has been widely studied. It is found that the initial column height–width aspect ratio dominates the flow regime.<sup>8–18</sup> However, for immersed granular collapse, due to its complicated granular dynamics and particle–fluid interactions, the immersed granular collapse is much less well studied. The flow is highly dependent on many factors, such as the fluid properties, particle diameter, and initial state, including the solid concentration and aspect ratio. Existing studies are mainly based on numerical simulations, including the Eulerian–Eulerian,<sup>19–24</sup> Eulerian–Lagrangian,<sup>7,25–33</sup> and Lagrangian–Lagrangian.<sup>34–36</sup> These numerical studies are based on relatively few experimental investigations.<sup>21,34,37–39</sup> The available experimental results are mainly from collapse events in the viscous regime, as shown in Fig. 1, and the inertial regime and transitional regime<sup>38</sup> have rarely been studied.

Moreover, researchers have mainly focused on the behavior of the granular phase, largely overlooking the fluid phase motion and particle–fluid interactions. Previous numerical investigations have found that the fluid vortex generated by particle motion will in turn drive the particles near the upper surface of the granular material, leading to the wavy shape of the granular morphology.<sup>21,23,30</sup>

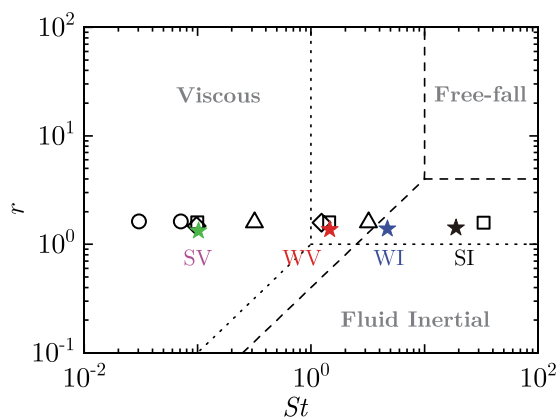


**FIG. 1.** Flow regime phase diagram. Stars, circles, squares, diamonds, and triangles correspond to the experiments performed in the present study and by Rondon *et al.*,<sup>37</sup> Bougouin and Lacaze,<sup>38</sup> Wang *et al.*,<sup>34</sup> and Lee *et al.*,<sup>21</sup> respectively. The dashed and dotted lines correspond to the boundaries of flow regimes proposed by Pont *et al.*<sup>3</sup> and Cassar *et al.*,<sup>4</sup> respectively.

However, these results actually lack experimental evidence. Available experiments concerning the fluid motion were conducted by Pinzon and Cabrera,<sup>40</sup> who studied planar granular collapse and added dye to the fluid to visualize the fluid motion using particle image velocimetry (PIV). However, only statistical analysis is applied in the column near region and the description is qualitative rather than quantitative. To date, there are no direct experimental results concerning the fluid flow details and its influence on the granular movement, especially in different flow regimes.

In this paper, we mainly focus on immersed granular collapse, that is, collapse in the inertial and viscous regimes, with an initially dense packing (solid concentration  $\alpha_s \approx 0.64$ ). Experiments are conducted over a wide range of  $St$  values, and new observation methods are introduced to ensure a comprehensive analysis of the individual collapse characteristics of both the particles and the fluid.

The remainder of this paper is organized as follows. We introduce the experimental setup, observation method, and experimental groups in Sec. II. The observations are described in Sec. III, mainly focusing on the collapse procedure of particles and fluid. Section IV presents a quantitative analysis of the collapse dynamics for different flow regimes. Finally, the conclusions to this study are summarized in Sec. V.

## II. EXPERIMENTAL PROCEDURE

### A. Granular material and fluid

The experiment is designed based on refraction index matching method.<sup>41,42</sup> Transparent borosilicate glass beads ( $d = 3.84 \pm 0.3$  mm) are chosen as the particles that have a measured density of  $2178 \text{ kg} \cdot \text{m}^{-3}$ . By gently dropping particles from a hopper onto a granular pile and measuring the edge slope using image processing,<sup>43</sup> the repose angle  $\theta_r$  is found to be about  $25^\circ$ . The friction coefficient between the particles and the wall,  $\mu_{p-w}$ , is determined by a sliding test,<sup>32</sup> which gives  $\mu_{p-w} = 0.19$ . The fluid is a mixture of dimethyl sulfoxide (DMSO) aqueous solution and glycerin aqueous solution. The solutions possess refractive index of 1.474, which matches with that of the borosilicate glass beads. These solutions have a similar density, but dramatically different viscosities (measured to be  $2.37 \text{ mPa} \cdot \text{s}$  for the DMSO solution and  $811 \text{ mPa} \cdot \text{s}$  for the glycerin solution). By mixing the two liquids properly, it is possible to perform experiments in different flow regimes as will be seen in Sec. II C.

### B. Experimental setup and imaging methods

The experimental setup for studying the immersed granular collapse is sketched in Fig. 2. A confining gate ( $\approx 3$  mm thick) is used to form a rectangular space in the corner of a glass water tank ( $50 \times 8 \times 40 \text{ cm}^3$ ). The particles are first wet with the fluid and then added with caution into the space in case of any trapped air. After then, a plate is used to press the granular block to its target height  $H_0$ . The initial width of the block is  $L_0 = 4$  cm and the height  $H_0$  is varied to form different aspect ratios as  $a = H_0/L_0$ . After the gate is removed vertically driven by a system of ropes and valleys, the granular column collapses onto the horizontal plane under gravity. The moment the gate starts to move is denoted as  $t = 0$  s. The duration of the gate-removal stage is less than one-tenth of the collapse duration (see Sec. IV B). Hence, the influence of the gate movement is believed to be minor and only exists in the initial stage.<sup>21–23,34</sup> A lid is placed on the liquid free surface to prevent any possible waves from forming when

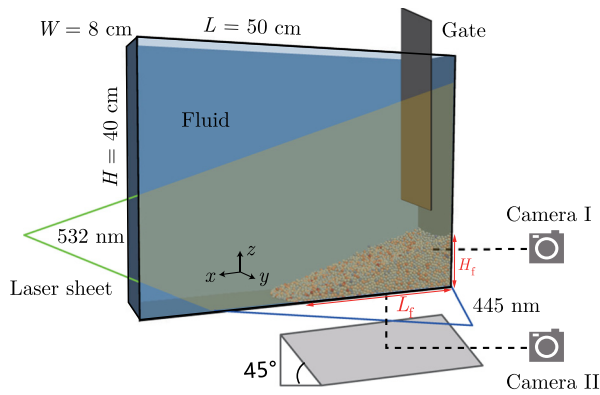


FIG. 2. Experimental setup of the immersed granular collapse.

the granular column starts to collapse and mimics a no-slip boundary condition.

The chosen particles are nearly transparent when immersed in the fluid due to the matched refractive index. To improve the contrast between the particles and the fluid, moderate Rhodamine 6G is dissolved in the liquid and a green laser sheet (thickness  $\approx 1$  mm, wavelength 532 nm) is illuminated from the left along the front wall within a distance of 3 mm to it, to lighten the fluid background with fluorescence (emission peak wavelength  $> 555$  nm). The fluid is also seeded with fluorescent tracer particles (named as tracers in the following), which give out brighter fluorescence. We use a black-and-white camera (camera I) with a resolution of  $2048 \times 2048$  pixels to record the collapse process at an acquisition rate of 50–1000 Hz, depending on the deformation rate in the different flow regimes. In this way, the particles and fluid tracers near the front wall are simultaneously recorded. The particles in the inner region are only observable when they come into the laser plane. Different with previous experiments, we also observe the motion of the bottom particles. A blue laser sheet (445 nm) is illuminated from the front along the bottom plate, and the scattered light of bottom particles is reflected to a photochromic camera (camera II) by a mirror placed under the tank, inclined at a  $45^\circ$  angle from the horizontal.

A bandpass filter (400–500 nm) enables camera II to capture the scattered blue laser only. For the postprocessing, only the blue channel of the obtained images is used. A high-pass filter (550 nm) located before camera I discards the source laser, so that camera I captures only the fluorescence. Thus, in the images obtained by camera I, the particles are dark and the tracers are bright points, while the fluid exhibits an intensity in between.

### C. Experimental groups

The mass fraction of glycerin in the fluid varies from 0 to 91%, and the corresponding viscosity varies from 2.37 to 411 mPa · s. Table I lists the fluid properties of the four groups considered in this investigation. For each group, the aspect ratio is varied from 2 to 6, and the experiment is repeated at least three times for each aspect ratio.

TABLE I. Parameters for each experimental group.

Fluid density ( $\text{kg} \cdot \text{m}^{-3}$ )	Fluid viscosity ( $\text{mPa} \cdot \text{s}$ )	( $St, r$ )	Regime	Label
1087	2.37	(19.04, 1.42)	Strongly inertial	SI
1139	9.37	(4.70, 1.38)	Weakly inertial	WI
1167	29.7	(1.46, 1.37)	Weakly viscous	WV
1235	411	(0.10, 1.33)	Strongly viscous	SV

According to Pont *et al.*,<sup>3</sup> the boundary between the viscous and inertial regimes is  $Re = St/r = 2.5$  and Bougouin and Lacaze<sup>38</sup> confirmed this conclusion. Our experiment gives two groups far away from this boundary, which indicates that they are in the strongly viscous (SV) or strongly inertial (SI) regime. The other two groups are near the boundary, implying that the viscous or inertial regimes are weak and that they are more likely to present the coexistence of the two regimes. Hence, we name these two groups the weakly viscous (WV) and weakly inertial (WI) regimes. The distribution of the four groups in the collapse regime diagram is shown in Fig. 1.

## III. EXPERIMENTAL RESULTS

### A. Granular collapse process

The collapse process is shown in Fig. 3 (Multimedia views) for the SI and SV regimes with initial aspect ratios of 2 and 5. For the SI regime, the collapse starts soon after the plate begins to move. The column height decreases rapidly and approaches the final height ( $\approx L_0$ ) at  $t = 0.6t_{95}$ , even for the high column with  $a = 5$ . Here,  $t_{95}$  is the time when the collapse runout approaches 95% of the total runout as used in previous studies<sup>37,38</sup> and see also the definition in Sec. IV B. The final deposition has a low height and long length, forming a sharp triangle, and possesses a depression near the right wall in the case of higher column collapse ( $a \geq 3$ ). We did not investigate higher column collapses because the runout may exceed the view range, and could even reach the left wall. From previous investigations,<sup>21,30,38</sup> the shape of the final deposition in the inertial regime tends to be more wavy and may resemble a Mexican hat for larger values of  $a$ .<sup>9</sup> This is mainly due to the fluid influences, which will be discussed in Sec. III C.

The SV regime collapses in a quite different manner to the SI regime. The collapse is much slower than in other groups. Within a few seconds after the gate is removed, the lower particles observed by camera I have barely moved, while the upper particles have destabilized and started moving prior to the lower ones. Though camera I only clearly records the first particle layer, it is still possible to observe that those indistinct inner particles drop first (see Fig. 3). Camera II provides more evidence that, after a few seconds of the gate leaving, some particles suddenly emerge near the bottom plate, while the initial bottom particles have not moved that far, as shown in Fig. 3 ( $t = 4.9 \text{ s} \approx 0.17t_{95}$  for  $a = 2$  and  $t = 7.8 \text{ s} \approx 0.39t_{95}$  for  $a = 5$  in SV regime). Thus, we can infer that, for the collapse in the SV regime, those upper-left corner particles drop first and arrive at the bottom plate, forming the collapse front prior to the lower particles. Because of the high viscosity, particles near the front wall are retarded by the boundary layer, while inner particles fall down leaving a single near-wall retarded layer, indicated by higher intensity due to loss of inner particles (see SV regime in Fig. 3). The upper particles gradually fall

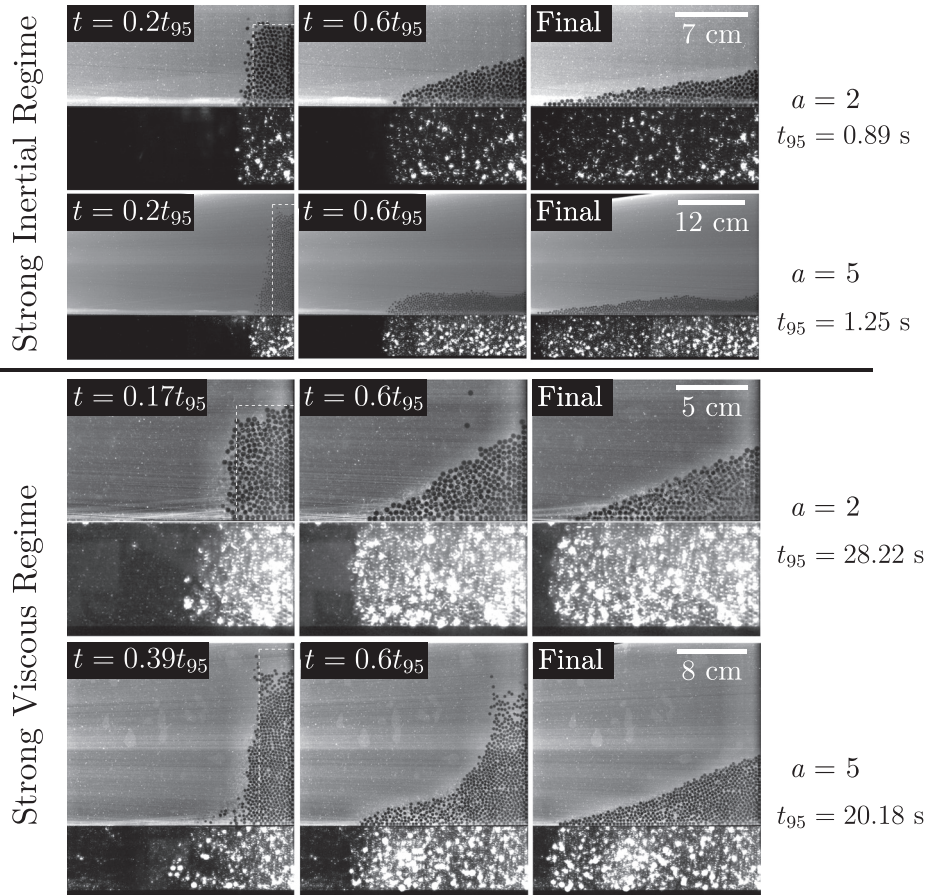


**FIG. 3.** Collapse process of SI and SV regimes with aspect ratios of  $a=2$  and  $a=5$ . For each instant, the upper and lower images are obtained from cameras I and II, respectively. The white lines in first column mark the initial state. See definition for  $t_{95}$  in Sec. 6. Multimedia views: <https://doi.org/10.1063/5.0067485.1>; <https://doi.org/10.1063/5.0067485.2>; <https://doi.org/10.1063/5.0067485.3>; <https://doi.org/10.1063/5.0067485.4>

down and move into the inner region, disappearing from the images of camera I. The final deposition is triangular for all aspect ratios.

Regime WI exhibits a similar collapse process as the SI regime, but the collapse proceeds more slowly and ends with a less sharp triangle. The depression, though less remarkable, is also observed in the WI regime for higher aspect ratios ( $a \geq 5$ ). The WV regime gives a triangular final deposition, similar to the SV regime. Generally speaking, a higher fluid viscosity results in a less mobile fluid and particles. In addition, the three dimensionality (see the Appendix A) is more pronounced at higher viscosity, manifested as retarded particles near the front wall. As a result, the particles making up the flow front observed by camera I actually spring up from the inner region. For the most viscous group (SV regime), in the final deposition, the particles within approximately  $0.5L_f$  from the final leading front are newly appeared, where  $L_f$  is the final deposition length.

The peculiar collapse characteristics of the SV regime, that is, particles drop to the bottom plate to form the flow front, are not apparent in other regimes. This phenomenon actually indicates that the movement of the bottom particles is so significantly retarded that the upper particles arrive at the bottom plate before the bottom particles have started moving. It has been reported by Rondon *et al.*<sup>37</sup> that initially dense and loose packing collapses in different manners. According to the critical state theory,<sup>44,45</sup> the dense (loose) packing must dilate (contract) before it can flow. A negative (positive) excess pore pressure

zone forms in the main body of the granular column, and this sucks in (ejects) fluid through the granular skeleton, which further stabilizes (destabilizes) the column,<sup>37,46</sup> resulting in the slow (fast) collapse process. We recall that all our experiments used an initially dense packing ( $\alpha_s \approx 0.64$ ). The different initial collapse manner of the SV regime compared with the other groups can be explained by the timescale  $t_{\text{relax}}$  required for the excess pore pressure to relax, which is inversely proportional to the hydraulic conductivity  $k$ ,<sup>45,47</sup>

$$t_{\text{relax}} = \frac{\rho_p}{\rho_p - \rho_f} \frac{\alpha_s - \bar{\alpha}_s}{\alpha_s \bar{\alpha}_s} \frac{L^*}{k}, \quad \text{where } k = \frac{(1 - \alpha_s)^3 d^2 \rho_f g}{\alpha_s^2 \mu_f}. \quad (4)$$

Here,  $L^*$  is the characteristic length and  $\bar{\alpha}_s$  is the solid concentration in the flowing layer, which are defined to be  $L^* = L_0/2$  and  $\bar{\alpha}_s = 0.58$  in this paper. Lower values of  $k$  mean that the fluid flows less easily through the granular skeleton, and so the pore pressure takes longer to relax. For the SV regime,  $t_{\text{relax}} = 12.83$  s, which is much longer than the time required for the upper-left particles to arrive at the bottom plate (4.9 and 7.8 s for  $a=2$  and  $a=5$ , respectively). During this relaxation time, the main body of the SV regime remains in its initial state, while the upper-left particles, which are less pressured and consolidated, become destabilized first.<sup>32,48</sup> While for the SI regime,  $t_{\text{relax}} = 0.06$  s, which is quite insignificant compared with the collapse duration ( $\approx 1$  s), so the pore pressure relaxation has little influence on

the collapse and the collapse is observed to start from the column foot. Thus, it can be concluded that the fluid viscosity significantly changes the initial collapse behavior. In fact, from Eq. (4),  $t_{\text{relax}}$  is also controlled by the solid concentration  $\alpha_s$  and particle diameter  $d$ , which may alter the collapse, as reported by Rondon *et al.*<sup>37</sup> and Lee *et al.*<sup>21</sup>

**B. Final runout and height**

In our experiment, most particles were involved in the collapse process because the columns are relatively high ( $a_{\text{min}} = 2$ ). The final depositions were generally triangular, although a depression may appear at the right part for inertial regimes. In particular, no trapezoidal-shaped deposition<sup>21,24,38</sup> was observed. In terms of the final deposition, the final length has long been of interest because of its geophysical meaning.  $L_f$  is defined here as the maximum distance the particles observed from camera I can reach, ignoring detached particles. Note that this length is reasonable because it reflects the movement of the granular pile, but not that of dispersed particles. The farthest position the particles can reach, as observed by camera II, is normally 1–2 cm beyond  $L_f$ . Figure 4(a) shows the normalized runout  $R^* = (L_f - L_0)/L_0$  with respect to the aspect ratio. The runout tends to increase with increasing aspect ratio and decreasing viscosity (SV and SI regime as the boundary).  $R^*$  obeys a power-law relationship with the aspect ratio as:  $R^* = \lambda a^\alpha$ . For the wide span of  $St$  in this study (0.1–19.04), the exponent  $\alpha$  does not vary significantly, remaining in the range 0.72–0.86, whereas the coefficient  $\lambda$  almost doubles, from  $\lambda_{\text{SV}} = 1.49$  to  $\lambda_{\text{SI}} = 2.37$ .

The final height  $H_f$  is defined as the height of deposition close to the right wall. The normalized final height  $H^* = H_f/L_0$  with respect to  $a$  is shown in Fig. 4(b) illustrating the remarkable differences among the different flow regimes. The final height of the SV regime follows the power-law relationship  $H^* = 0.88a^{0.53}$ .  $H_f$  in the WV regime is lower than in the SV regime, and the difference tends to increase for larger values of  $a$ .  $H_f$  in the SI regime is approximately the initial length  $L_0$  ( $H^* \approx 1$ ), indicating that the increased upper particles are transported to a longer distance, leaving a depression whose height is nearly  $L_0$ . For higher values of  $a$ ,  $H_f$  even tends to decrease, implying that the transport effect grows stronger. A similar trend was also observed by Bougouin and Lacaze,<sup>38</sup> Jing *et al.*,<sup>30</sup> and Lee *et al.*<sup>21</sup> For

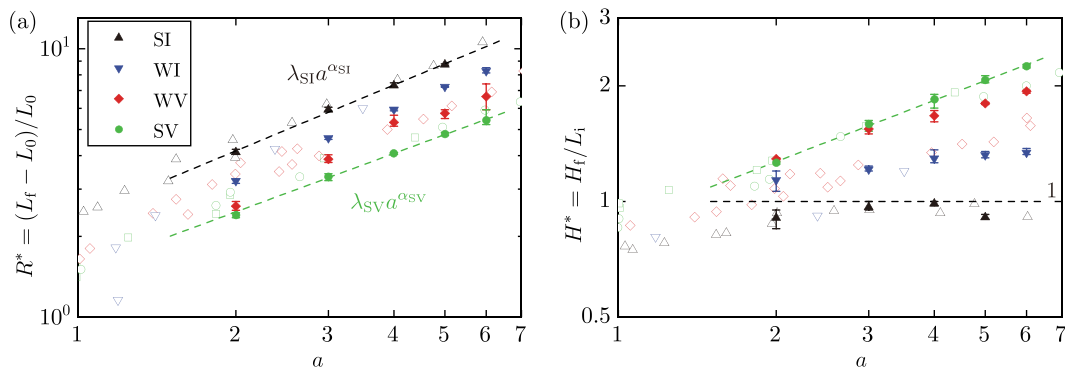
the WV regime,  $H_f$  is higher than in the SI regime. With increasing  $a$ ,  $H_f$  tends to achieve a constant value, at which the depression appears, and this value is higher than that of the SI regime.

Figure 4 also presents the experimental results from previous investigations.<sup>21,37,38</sup> Note that the results from different regimes may give significant differences, so we only compare the results with similar regime indicated by Fig. 1. The results with close ( $St, r$ ) are marked with same color and generally same edge profile as shown in Fig. 4. It can be seen that the results for the SI and SV regime for both final length and height agree well with those reported by Bougouin and Lacaze<sup>38</sup> and Rondon *et al.*<sup>37</sup> ( $\alpha_s = 0.60$ ). The WV regime exhibits close final length with Bougouin and Lacaze<sup>38</sup> but slightly larger final height. The results by Lee *et al.*<sup>21</sup> are also comparable with the WI regime results given by this paper. All in all, our experimental results generally match well with previous results by different researchers and in different flow regimes.

Note that a wide distribution of flow width  $W$  exists in previous investigations, for example,  $667d$  in Rondon *et al.*,<sup>37</sup>  $357d$  in Lee *et al.*,<sup>21</sup> and  $67d$  in Bougouin and Lacaze,<sup>38</sup> compared with our width  $\approx 20d$ . Since the final runout and height are well comparable between them and this study, we believe that the chosen width is enough to represent a typical immersed granular collapse process. Future systematic investigations on the influence of  $W$  on the collapse process are still deserving.

**C. Particles and fluid motion**

The fluid tracers are recorded by camera I as bright dots and can be tracked using particle tracking velocimetry (PTV). In this study, the open-source PTV code TracTrac<sup>49</sup> is used to determine the position and displacement of each tracer. To enhance the contrast between the tracers and the fluid, the background (determined by averaging 10 frames forward and backward, i.e., 21 frames in total) is subtracted from the original image of every frame. The fluid motion is represented by the tracers' trajectories. For each instant investigated, tracers recognized in the past tens of frames are indicated by scattered points that are colored according to their velocity magnitude. The point size increases as the frame gets closer to that instant. Only tracers that can be continuously tracked for at least ten frames are shown. In addition,



**FIG. 4.** (a) Normalized final runout and (b) normalized final height against aspect ratio  $a$ . The filled markers are the experimental results in this paper. The hollow markers are the experimental results obtained by Bougouin and Lacaze<sup>38</sup> ( $\triangle, \diamond, \circ$ ), Lee *et al.*<sup>21</sup> ( $\nabla$ ), and Rondon *et al.*<sup>37</sup> ( $\square$ ), compared with SV). The markers with the same color and edge profile possess close ( $St, r$ ). The dashed lines correspond to the power-law fit of the experimental results. The error bars represent the maximum and minimum values of at least three repetitions under the same experimental conditions (as in subsequent figures).

the particles are also tracked with PTV based on the Hough transform circular detection and nearest-neighbor matching methods.<sup>50,51</sup>

### 1. Overview of the motion

Figure 5 (Multimedia view) shows the fluid motion of the SI regime with  $a=4$ . After the gate is lifted, the particles start to fall down, driving the stationary fluid downward, while the collapse front pushes the fluid forward, generating a large recirculation of the ambient fluid, as shown in Figs. 5(a)–5(c). With the continuous falling of particles, a large vortex (vortex A) builds up at the upper-left corner of the column, as shown in Fig. 5(b). Vortex A is generally located above the column top and near the right wall. During the falling process, vortex A descends with the granular collapse and swirls the upper particles. As the pile front invades the fluid ahead, another small vortex (vortex B) builds up in the region encircled by the recirculation and vortex A, as shown in Fig. 5(c). Vortex B is located above the front and closely follows the front movement. At  $t = 0.65t_{95}$  when the upper particles generally arrive at their final height ( $\approx L_0$ ), the particles beneath vortex A are picked up and thrown to the front region, leaving a depression. Vortex A then crosses over the depression and moves forward, transporting the particles beneath it further ahead. In the later stages of the collapse, the recirculation almost disappears, while the two vortices continue to develop and move forward under the fluid inertia, as shown in Fig. 5(d). In general, for higher columns, the intensity of vortex A is stronger, resulting in a deeper depression. This is the

reason for the final height decreasing, as shown in Fig. 4(b). Vortices A and B also exist in the WI regime, although they are much weaker because of the increased viscosity, which depresses the fluid inertia.

The fluid motion of the WV regime with  $a=4$  is shown in Fig. 6 (Multimedia view). The recirculation is similar to that in inertial regimes. Above the granular column, the fluid mainly heads downward following the falling particles, as shown in Fig. 6(b). Most of the fluid motion occurs near the granular pile and follows the granular flow direction, but the vortices cannot be clearly distinguished. In addition, the fluid velocity is about three times smaller than that of the SI regime, and no particles appear to be picked up by the fluid, which explains the triangular final deposition in the viscous regime. Similar results can be observed more clearly in our previous investigation of the WV regime using CFD-DEM simulations<sup>32</sup> (note that the large vortex described there is actually the recirculation proposed here). The SV regime exhibits the weakest fluid motion, which is only obvious near fast-moving particles. Readers are referred to the videos accompanying Fig. 3 for the flow details.

### 2. The relative motion of particles and fluid

In the immersed granular collapse, the fluid drag  $F_d = C_d \pi d^2 \rho_f |\mathbf{u}_f| \mathbf{u}_f / 8$  plays a significant role in changing the collapse manner. The relative velocity between the fluid and particles  $\mathbf{u}_r = \mathbf{u}_f - \mathbf{u}_p$  determines the direction and magnitude of  $F_d$ . During the initial stage of collapse, the falling particles are enduring negative

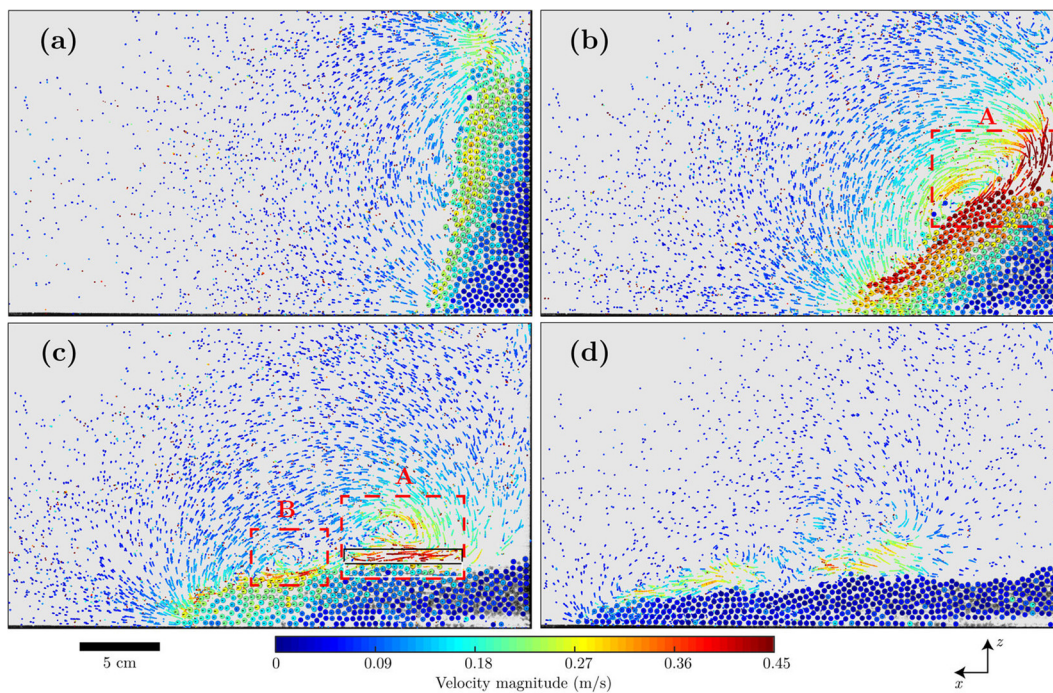


**FIG. 5.** Trajectory of fluid tracers and velocity of particles in SI regime with aspect ratio  $a=4$  at (a)  $t = 0.2t_{95}$ , (b)  $t = 0.4t_{95}$ , (c)  $t = 0.65t_{95}$ , and (d)  $t = t_{95}$ . The PTV-tracked tracers and particles are represented by small dots and circles, respectively, and colored by their velocity magnitude according to the same color bar. Tracers in a total of 40 frames (0.04 s) before each instant are shown. The short lines associated with the particles indicate the velocity direction, with the length scaled by the velocity magnitude. Dashed rectangles A and B designate the vortices described in the text. Black and white rectangles in (c) are the regions used for velocity averaging for tracers and particles, respectively. Multimedia view: <https://doi.org/10.1063/5.0067485.5>

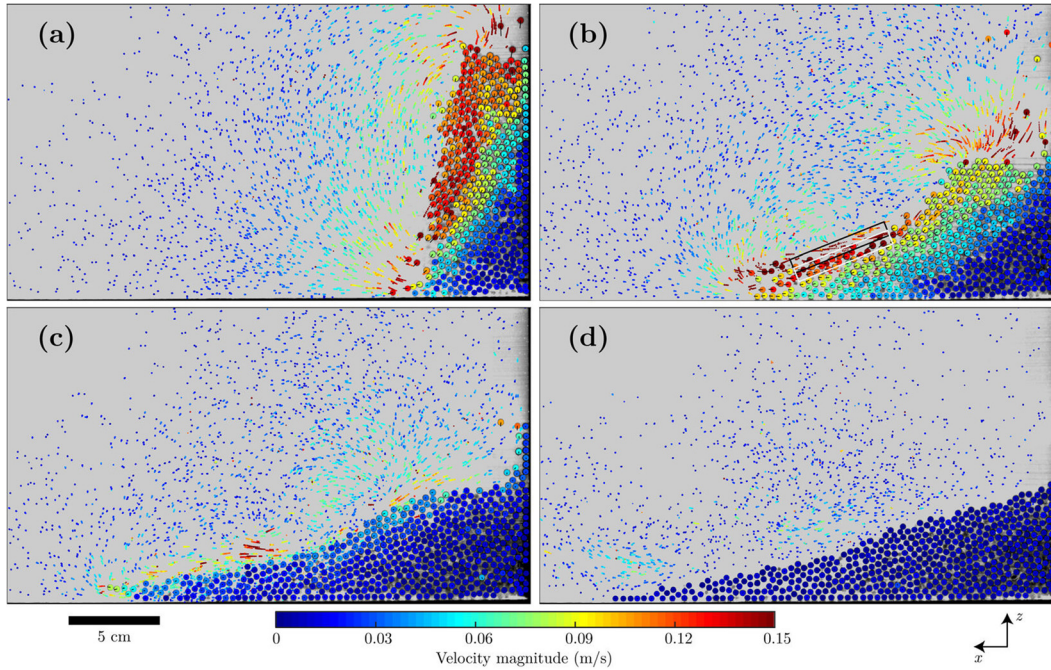


**FIG. 6.** Trajectory of fluid tracers and velocity of particles in WV regime with aspect ratio  $a = 4$  at (a)  $t = 0.4t_{95}$ , (b)  $t = 0.75t_{95}$ , (c)  $t = t_{95}$ , and (d)  $t = 2t_{95}$ . Tracers in a total of 10 frames (0.04 s) before each instant are shown. The motion representation is the same as in Fig. 5. Black and white rectangles in (b) are the regions used for velocity averaging for tracers and particles, respectively. Multimedia view: <https://doi.org/10.1063/5.0067485.6>

fluid drag since the fluid is initially static. In the later stage, the particles almost stop moving, while the fluid is still flowing indicating that the particles are enduring positive drag force, which helps their further transport. Therefore, there should be a stage when the role of the fluid on the particles transfers from resistance to driving, indicated by a negative to positive value of  $\mathbf{u}_t \cdot \mathbf{u}_p$ .

Here, we give a rough but still meaningful investigation on the relative velocity near the surface of the granular pile. We study the moment of  $0.65t_{95}$  for the SI regime and  $0.75t_{95}$  for the SV regime as shown in Figs. 5(c) and 6(b), respectively. These two moments correspond to the ends of the steady propagation stage as will be defined in Sec. IV C. The investigated regions are marked with black rectangle for tracers and white rectangle for particles. The rectangles have a dimension of approximately  $2d \times 15d$ . The averaged velocity of tracers  $\bar{\mathbf{u}}_t = (\bar{u}_{t,x}, \bar{u}_{t,z})$  and particles  $\bar{\mathbf{u}}_p = (\bar{u}_{p,x}, \bar{u}_{p,z})$  in the specific region are used to calculate  $\mathbf{u}_r$ . It can be seen that the tracers and fluid regions used are near but not totally coincident, which we believe is still acceptable.

The obtained results based on the averaged methods are given in Table II for SI and WV regimes. Here, the drag force coefficient is calculated by Schiller–Naumann equation<sup>52</sup>  $C_d = 24(1 + 0.15Re_p^{0.687}/Re_p)$ .

**TABLE II.** Results of the velocities and forces for SI and WV regimes.

	$\bar{\mathbf{u}}_t$ (m/s)	$\bar{\mathbf{u}}_p$ (m/s)	$\bar{\mathbf{u}}_r$ (m/s)	$F_d$ (N)	$f$ (N)
SI, $a = 4$	(−0.332, −0.011)	(−0.172, −0.023)	(−0.160, 0.012)	$1.13 \times 10^{-4}$	$1.48 \times 10^{-4}$
WV, $a = 4$	(−0.156, −0.028)	(−0.141, −0.034)	(−0.014, 0.006)	$2.05 \times 10^{-5}$	$1.37 \times 10^{-4}$

The friction force is estimated by  $f \sim G \tan \theta_r$  with  $G = (\rho_p - \rho_f)g\pi d^3/6$  being the particle’s reduced gravity. The results indicate that the drags of the SI and WV regimes both act positively to the particles ( $\mathbf{u}_t \cdot \bar{\mathbf{u}}_p > 0$ ). The drag force of the SI regime is comparable with the particle’s friction force, so the fluid drag may significantly help the particles’ further transport, which results in the formation of the depression. The relative velocity of the WV regime is one magnitude smaller than that of SI regime. The drag of the WV regime is seven times smaller than the granular friction, so it is concluded that the fluid is mainly flow following the particles and the fluid drag here is quite less positive.

#### IV. ANALYSIS AND DISCUSSION

In this section, we analyze the collapse dynamics based on the front propagation. Because the particles observed by camera I may be retarded, we judge the front position from camera II. At instant  $t$ , the front position of the bottom particles  $L_f$  is where the summation of the transverse intensity of the image achieves a given threshold. The threshold is experiment-dependent, but is approximately 1/4 the maximum intensity.



It is widely agreed that the final runout  $R_f = L_f - L_0$  generally evolves in three stages, that is, acceleration, steady propagation, and deceleration.<sup>19,21,32,39</sup> The collapse starts from a static state and the particles fall down to drive the surrounding fluid into motion. As a result, the granular potential energy is converted into the kinetic energy of the particles and fluid, and the collapse accelerates. As the granular velocity increases, the driving forces (mainly the pressure gradient) approximately balance the resistance (mainly interparticle friction and drag force, which depends on the relative velocity), and the front propagates with a relatively steady velocity.<sup>19</sup> In the later stage, the particles arrive at their final height and the driving forces weaken, leading to the front's deceleration.

Given the peculiar collapse behavior of the SV regime, the front position is difficult to determine in the first half of the total runout. Thus, this regime is omitted from the analysis of the acceleration and steady propagation stages.

### A. Acceleration stage

In the case of dry granular collapse, Lube *et al.*<sup>11</sup> found that the acceleration during the initial stage remains constant, that is,  $0.75g'$ . For the immersed case, Jing *et al.*<sup>30</sup> found a similar result:  $0.75g'$ , where  $g' = (\rho_p - \rho_f)g/\rho_p$  is the reduced gravity. In this paper, we assume that the acceleration is  $\beta g'$ . The runout evolutions for all experiments in the SI, WI, and WV regimes are shown in the insets of Fig. 7. The sampling stage to determine  $\beta$  is about 10% of the total runout. We find that the coefficient  $\beta$  is highly dependent on the fluid viscosity and the aspect ratio. For the same regime,  $\beta$  tends to increase with increasing aspect ratio, and the upper/lower limits of  $\beta$  are 0.15/0.25 for the SI regime, 0.05/0.14 for the WI regime, and 0.015/0.04 for the WV regime. Generally,  $\beta$  decreases with increasing fluid viscosity (decreasing  $St$ ). In fact, for the extreme situation in which the fluid viscosity goes to infinity, the granular materials barely move and  $\beta$  tends to zero.  $\beta$  may be related to many factors, such as the fluid viscosity (as reported here), particle size distribution, interparticle contacts, initial packing density, and aspect ratio. A proper prediction of  $\beta$  requires systematic investigation and would be meaningful for disaster prevention and risk assessments.

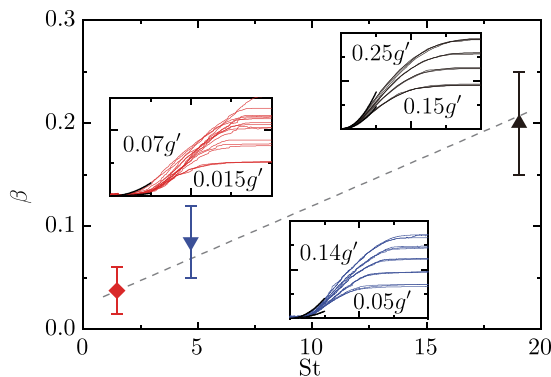


**FIG. 7.** Acceleration coefficient  $\beta$  vs  $St$ . Black, blue, and red markers correspond to the SI, WI, and WV regimes, respectively. The insets are the runout evolutions of different regimes. The black short curves denote the ideal acceleration, that is,  $\beta g' t^2 / 2$ . The dashed line provides a visual guide.

### B. Collapse duration and regime analysis

For each experiment, we define the length scale  $L_{95}$  satisfying  $L_{95} - L_0 = 0.95(L_f - L_0)$  and the timescale  $t_{95}$  as the time at which the front particles reach  $L_{95}$ . We consider  $t_{95}$  as the collapse duration, because in later stages, the granular pile collapses quite slowly and the presence of some detached moving particles makes it difficult to determine a proper total collapse time. In general, with a more viscous fluid, the granular pile will take longer time to fully stop moving after reaching  $L_{95}$ . For the SV regime, we waited more than 10 min to get the final deposition shown in Fig. 3, whereas  $t_{95}$  is just tens of seconds.

Figure 8 shows the variation of  $t_{95}$  for the different regimes. For the SI, WI, and WV regimes, the collapse duration grows longer with increasing aspect ratio, which is in line with intuition. The SI and WI regimes have similar  $t_{95}$  values, although there are significant differences in their runout as shown in Fig. 4(a). However, for the SV regime,  $t_{95}$  remains almost constant, despite the runout growing longer for higher aspect ratios. This is because the creep behavior in the later stage takes up most of the collapse duration, and higher column collapses exhibit larger velocities, which imply a faster creep stage.

Following Bougouin and Lacaze,<sup>38</sup> we introduce characteristic timescales defined as

$$t_V = \frac{H_0}{U_V^\infty}, \quad t_I = \frac{H_0}{U_I^\infty}, \quad t_{FF} = \frac{H_0}{U_{FF}}, \quad (5)$$

where

$$U_V^\infty = \frac{(\rho_p - \rho_f)gd^2}{18\mu_f}, \quad U_I^\infty = \sqrt{\frac{4(\rho_p - \rho_f)gd}{3C_d\rho_f}}, \quad (6)$$

are the viscous and inertial regime terminal velocities, respectively, for a falling particle in fluid when the hydrodynamic forces (mainly drag force) balance the reduced gravity and the velocities only depend on the material properties. In  $U_I^\infty$ ,  $C_d = 0.4$ .  $U_{FF} = \sqrt{2g'H_0}$  is the velocity of a particle freely falling from a height of  $H_0$  under reduced gravity. The nearness of the collapse duration  $t_{95}$  with the characteristic timescales may identify the corresponding flow regime. Here, we discard the  $t_{FF}$ -normalization because it generally deviates from unity, which means that the experiment in this paper is by no means in the free fall regime. Figure 9 presents values of  $t_{95}$  normalized by  $t_V$  and  $t_I$ .

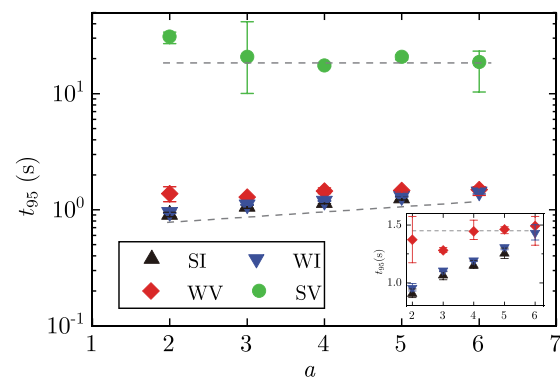


**FIG. 8.** Collapse duration  $t_{95}$  against aspect ratio  $a$  for different regimes. The dashed lines are visual guides.

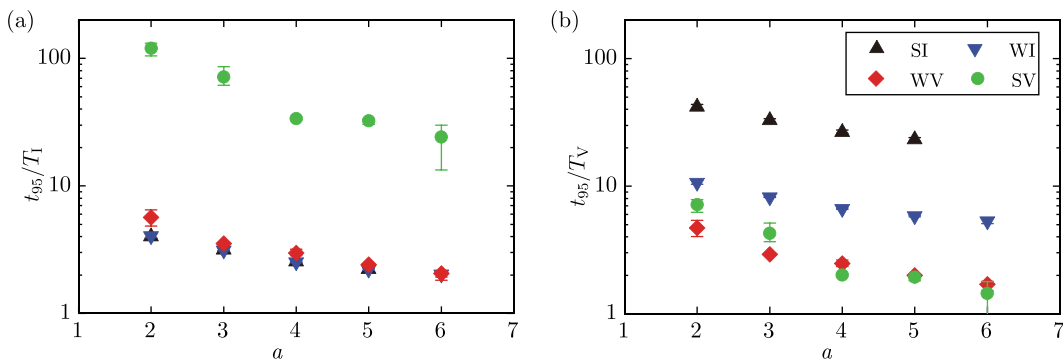


FIG. 9. Normalized runout duration by (a)  $t_t$  and (b)  $t_v$  against aspect ratio  $a$  for different regimes.

It can be seen that, as the aspect ratio increases, the normalization generally tends to unity, which proves that the regime characteristics are more pronounced for higher columns because the particles can move over longer distances to reach their limit velocity, which will be discussed in Sec. IV C. For the SI and WI regimes,  $t_t$ -normalization gives results that are the closest to unity, whereas  $t_v$ -normalization gives much larger values. Therefore, both the SI and WI regimes clearly correspond to inertial regime flows. Similar analysis also demonstrates that the SV regime is clearly viscous. For the WV regime, however,  $t_t$ -normalization and  $t_v$ -normalization are both close to unity, indicating that this regime exists near the boundary of the viscous and inertial regimes. Thus, the WV regime can be seen as the transitional state between the viscous and inertial regimes. Note that  $Re = St/r \approx 1.07$  for the transitional regime, which is in agreement with the value proposed by Cassar *et al.*<sup>4</sup>

### C. Steady propagation velocity and free fall scaling

By normalizing the runout using  $L_{95} - L_0$  and the time using  $t_{95}$ , we find that the curves for the same regime generally have a similar trend. As shown in Fig. 10, although it is difficult to distinguish the steady propagation stage from the collapse procedure precisely, we define the steady propagation stage, which possesses a constant slope

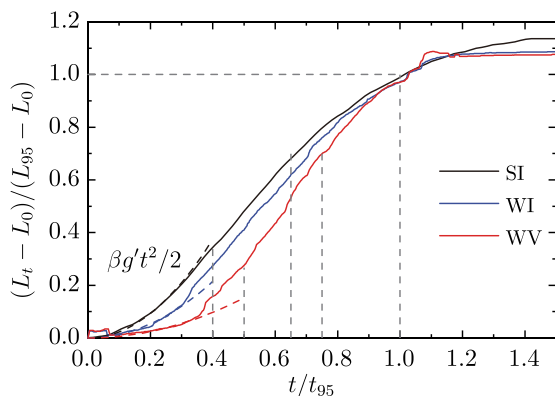


FIG. 10. Typical normalized runout evolution in different flow regimes.

between  $0.4$  and  $0.65t_{95}$  for the SI and WI regimes and  $0.5$ – $0.75t_{95}$  for the WV regime. The constant velocity  $U_c$  comes from a linear fit of the runout data during the steady propagation stage with coefficient of determination  $R^2 > 0.99$  for all the groups investigated.

As shown in Fig. 11(a),  $U_c$  increases with increasing aspect ratio for  $a \leq 4$  and tends to approach a saturated value for large aspect ratio. Note that for one single particle free falling in fluid, the particle will ideally achieve a certain terminal velocity. The initial falling process of the particles is quite similar to the free falling especially for higher columns where the particles have longer distance to fall, so, with the column height increasing, the falling particles will also tend to reach a limit velocity with no further acceleration. Therefore, when the particles approach the corner dead zone which forms an inclined plane and their velocity turns from vertical to horizontal, the crash velocity is stable and the particles motion changes to horizontal with similar speed. The driving force of the front particles is mainly the momentum of back-transferred particles, which is why the propagation velocity no longer increases.

To confirm the above conjecture, we study the averaged velocity  $U_{average}$  of the fastest 10% of particles in each instant from the PTV result, as presented in Sec. III C. These particles are generally located at the upper front side of the granular pile. The variation of  $U_{average}$ , during which time it generally reaches its maximum, is shown in Figs. 11(b)–11(d). As the aspect ratio increases,  $U_{average}$  tends to reach a constant value in the WV regime as shown in Fig. 11(d), which represents the limit velocity for the falling particles. Although the limit velocity does not seem to be achieved in the SI and WI regimes, the difference between neighboring aspect ratios is decreasing similar with the trend of  $U_c$ . Note that this limit velocity does not have to be the theoretical terminal velocity  $U_{V(1)}^\infty$  for one falling particle, because in the finite flow region, the ambient fluid will flow following the particles, which reduces the relative velocity and hence the drag force, and we also have to consider the wake effects of the neighboring particles. For the inertial regimes,  $U_{average}$  even grows higher than  $U_1^\infty$  as shown in Fig. 11(b). This fact is a further evidence that the fluid may help transport the particles.

### V. CONCLUSION

We have experimentally studied immersed granular collapse in different flow regimes. By introducing the refraction index matching

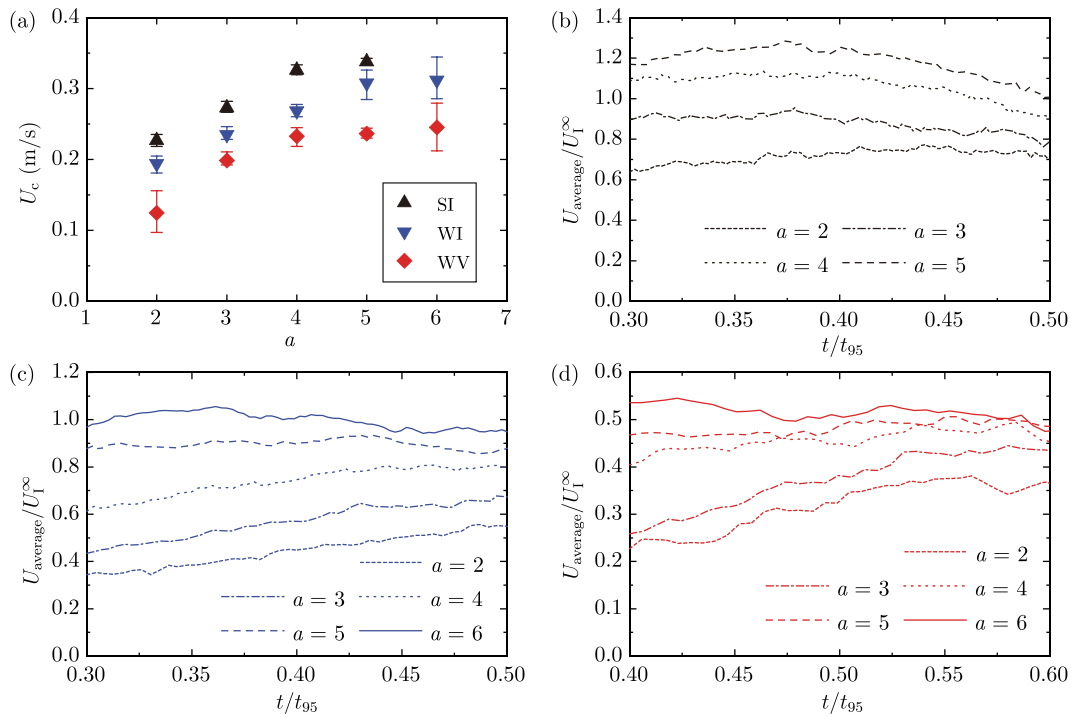


FIG. 11. (a) Front velocity against aspect ratio during the steady propagation stage. Averaged velocity variation for (b) SI regime, (c) WI regime, and (d) WV regime.

method and tracers into the fluid, the motion of the particles and the fluid was observed simultaneously. In addition, the propagation of the bottom particles was observed using a mirror placed below the experimental equipment. We found that the collapse behavior is significantly dependent on the initial column height–width aspect ratio as well as on the flow regime, which is mainly controlled by the fluid properties. The inertial regimes collapse faster, end with sharper final depositions, and have depressions near the right wall in the case of high columns, whereas the viscous regimes collapse more slowly and end with a pure triangular final deposition. In the SV regime, the collapse starts from the upper-left corner, from where particles drop to the bottom plate to form the flow front in advance of the bottom particles, which can be explained by the excess pore pressure relaxation time. For the inertial regimes, the swirling of the fluid is significant and may transport particles ahead, resulting in the depression. For higher-viscosity fluids, the fluid inertia is less pronounced and the fluid mainly follows the granular motion, leaving a pure triangular final deposition.

By comparing  $t_{95}$  with the characteristic timescales, we have found that the SI and WI (SV) regimes are clearly inertial (viscous) regimes, whereas the WV regime is close to the boundary of inertial and viscous regimes and possesses some unique characteristics of both, such as a similar propagation velocity and collapse duration to the inertial regimes, and the reduced fluid swirling and triangular-shaped final deposition of the viscous regime. As the aspect ratio increases, the collapse characteristics become more pronounced, and the collapse duration tends to the characteristic timescale of the particulate regime. The steady propagation velocity  $U_c$  tends to be constant for higher aspect ratios, as the falling particles reach a regime-

dependent limit velocity, indicating that the collapse will not accelerate all the way with increasing height.

DATA AVAILABILITY

The data that support the findings of this study are available from the corresponding authors upon reasonable request.

ACKNOWLEDGMENTS

The authors are grateful for the support of the National Natural Science Foundation of China (Grant Nos. 12032005 and 12172057). We thank Stuart Jenkinson, Ph.D., for editing the English text of a draft of this manuscript.

AUTHOR DECLARATIONS

Author Contributions

Y.S. and W.Z. contributed equally to this work.

APPENDIX: ON THE THREE-DIMENSIONALITY OF THE COLLAPSE

The three dimensionality due to sidewall has long bothered the studies of granular flow.<sup>47,53</sup> The wall effects during the immersed granular collapse are twofold, the higher drag on particles due to the fluid boundary layer and the friction between particles and wall. Hence, we may observe the retarded layer near wall, which refers to the near-wall region where only one single particle layer exists. This implies that the inner region flows fast than near-wall region.

We have to admit that the three-dimensionality effect is inelible especially for collapse in fluid with higher viscosity (SV regime). Yet in terms of a few problems we studied, we believe the results are still reasonable. For the final deposition, the profiles of the boundary and inner particles differ  $1d$  at most, because no retarded layer is observed finally. The collapse dynamics investigated in Sec. IV are based on the front propagation judged from camera II, that is, the leading position of the inner particles where the wall effect is less significant. The particles and fluid motion in Sec. III C is near front wall and actually cannot represent the inner flow, since the velocity vectors may be smaller and distorted near wall. Yet, we assume that the flow is vertically planar, and the motion on the same plane recorded by camera I can still reflect the flow and interaction pattern of particles and fluid in inner region.

## REFERENCES

- <sup>1</sup>K. Huhn, M. Arroyo, A. Cattaneo, M. A. Clare, E. Garcia, C. B. Harbitz, S. Krastel, A. Kopf, F. Lvholt, and M. Rovere, "Modern submarine landslide complexes: A short review," in *Submarine Landslides: Subaqueous Mass Transp. Deposits from Outcrops to Seismic Profiles* (American Geophysical Union, 2019), pp. 181–200.
- <sup>2</sup>S.-K. Hsu, J. Kuo, C.-L. Lo, C.-H. Tsai, W.-B. Doo, C.-Y. Ku, and J.-C. Sibuet, "Turbidity currents, submarine landslides and the 2006 PingTung earthquake off SW Taiwan," *Terr. Atmos. Ocean. Sci.* **19**, 767 (2008).
- <sup>3</sup>S. Courrech du Pont, P. Gondret, B. Perrin, and M. Rabaud, "Granular avalanches in fluids," *Phys. Rev. Lett.* **90**, 044301 (2003).
- <sup>4</sup>C. Cassar, M. Nicolas, and O. Pouliquen, "Submarine granular flows down inclined planes," *Phys. Fluids* **17**, 103301 (2005).
- <sup>5</sup>W. R. A. Goossens, "Review of the empirical correlations for the drag coefficient of rigid spheres," *Powder Technol.* **352**, 350–359 (2019).
- <sup>6</sup>V. Armenio and V. Fiorotto, "The importance of the forces acting on particles in turbulent flows," *Phys. Fluids* **13**, 2437–2440 (2001).
- <sup>7</sup>L. Jing, G. C. Yang, C. Y. Kwok, and Y. D. Sobral, "Flow regimes and dynamic similarity of immersed granular collapse: A CFD-DEM investigation," *Powder Technol.* **345**, 532–543 (2019).
- <sup>8</sup>E. Lajeunesse, A. Mangeney-Castelnau, and J. P. Vilotte, "Spreading of a granular mass on a horizontal plane," *Phys. Fluids* **16**, 2371–2381 (2004).
- <sup>9</sup>E. Lajeunesse, J. B. Monnier, and G. M. Homsy, "Granular slumping on a horizontal surface," *Phys. Fluids* **17**, 103302 (2005).
- <sup>10</sup>G. Lube, H. E. Huppert, R. S. J. Sparks, and M. A. Hallworth, "Axisymmetric collapses of granular columns," *J. Fluid Mech.* **508**, 175–199 (2004).
- <sup>11</sup>G. Lube, H. E. Huppert, R. S. Sparks, and A. Freundt, "Collapses of two-dimensional granular columns," *Phys. Rev. E* **72**, 041301 (2005).
- <sup>12</sup>N. J. Balmforth and R. R. Kerswell, "Granular collapse in two dimensions," *J. Fluid Mech.* **538**, 399–428 (2005).
- <sup>13</sup>L. Staron and E. J. Hinch, "The spreading of a granular mass: Role of grain properties and initial conditions," *Granul. Matter* **9**, 205–217 (2007).
- <sup>14</sup>L. Lacaze, J. C. Phillips, and R. R. Kerswell, "Planar collapse of a granular column: Experiments and discrete element simulations," *Phys. Fluids* **20**, 063302 (2008).
- <sup>15</sup>L. Girolami, V. Hergault, G. Vinay, and A. Wachs, "A three-dimensional discrete-grain model for the simulation of dam-break rectangular collapses: Comparison between numerical results and experiments," *Granul. Matter* **14**, 381–392 (2012).
- <sup>16</sup>E. Kermani, T. Qiu, and T. Li, "Simulation of collapse of granular columns using the discrete element method," *Int. J. Geomech.* **15**, 04015004 (2015).
- <sup>17</sup>C.-H. Lee, Z. Huang, and Y.-M. Chiew, "A three-dimensional continuum model incorporating static and kinetic effects for granular flows with applications to collapse of a two-dimensional granular column," *Phys. Fluids* **27**, 113303 (2015).
- <sup>18</sup>X. Xu, Q. Sun, F. Jin, and Y. Chen, "Measurements of velocity and pressure of a collapsing granular pile," *Powder Technol.* **303**, 147–155 (2016).
- <sup>19</sup>C. Meruane, A. Tamburrino, and O. Roche, "On the role of the ambient fluid on gravitational granular flow dynamics," *J. Fluid Mech.* **648**, 381–404 (2010).
- <sup>20</sup>S. B. Savage, M. H. Babaei, and T. Dabros, "Modeling gravitational collapse of rectangular granular piles in air and water," *Mech. Res. Commun.* **56**, 1–10 (2014).
- <sup>21</sup>C.-H. Lee, Z. Huang, and M. L. Yu, "Collapse of submerged granular columns in loose packing: Experiment and two-phase flow simulation," *Phys. Fluids* **30**, 123307 (2018).
- <sup>22</sup>C.-H. Lee and Z. Huang, "A two-phase flow model for submarine granular flows: With an application to collapse of deeply-submerged granular columns," *Adv. Water Resour.* **115**, 286–300 (2018).
- <sup>23</sup>P. Si, H. Shi, and X. Yu, "Development of a mathematical model for submarine granular flows," *Phys. Fluids* **30**, 083302 (2018).
- <sup>24</sup>M. L. Rocca, P. Prestinini, L. Elango, R. Hinkelmann, and A. Montessori, "Depth averaged modelling of loose rectangular granular piles collapsing in water," *Adv. Water Resour.* **143**, 103663 (2020).
- <sup>25</sup>V. Topin, F. Dubois, Y. Monerie, F. Perales, and A. Wachs, "Micro-rheology of dense particulate flows: Application to immersed avalanches," *J. Non-Newtonian Fluid Mech.* **166**, 63–72 (2011).
- <sup>26</sup>V. Topin, Y. Monerie, F. Perales, and F. Radja, "Collapse dynamics and runoff of dense granular materials in a fluid," *Phys. Rev. Lett.* **109**, 188001 (2012).
- <sup>27</sup>K. Kumar, J. Y. Delenne, and K. Soga, "Mechanics of granular column collapse in fluid at varying slope angles," *J. Hydrodyn.* **29**, 529–541 (2017).
- <sup>28</sup>K. Kumar, K. Soga, and J.-Y. Delenne, "Collapse of tall granular columns in fluid," *EPJ Web Conferences* **140**, 09041 (2017).
- <sup>29</sup>E. Izard, L. Lacaze, T. Bonometti, and A. Pedrono, "Numerical modeling of a granular collapse immersed in a viscous fluid," in *Advances in Hydroinformatics: Simhydro 2017—Choosing the Right Model in Applied Hydraulics* (Springer-Verlag Singapore Pte Ltd, 2018), pp. 1099–1116.
- <sup>30</sup>L. Jing, G. C. Yang, C. Y. Kwok, and Y. D. Sobral, "Dynamics and scaling laws of underwater granular collapse with varying aspect ratios," *Phys. Rev. E* **98**, 042901 (2018).
- <sup>31</sup>G. C. Yang, L. Jing, C. Y. Kwok, and Y. D. Sobral, "A comprehensive parametric study of LBM-DEM for immersed granular flows," *Comput. Geotech.* **114**, 103100 (2019).
- <sup>32</sup>Y.-H. Sun, W.-T. Zhang, X.-L. Wang, and Q.-Q. Liu, "Numerical study on immersed granular collapse in viscous regime by particle-scale simulation," *Phys. Fluids* **32**, 073313 (2020).
- <sup>33</sup>L. Lacaze, J. Bouteloup, B. Fry, and E. Izard, "Immersed granular collapse: From viscous to free-fall unsteady granular flows," *J. Fluid Mech.* **912**, A15 (2021).
- <sup>34</sup>C. Wang, Y. Wang, C. Peng, and X. Meng, "Dilatancy and compaction effects on the submerged granular column collapse," *Phys. Fluids* **29**, 103307 (2017).
- <sup>35</sup>C. Wang, Y. Wang, C. Peng, and X. Meng, "Two-fluid smoothed particle hydrodynamics simulation of submerged granular column collapse," *Mech. Res. Commun.* **79**, 15–23 (2017).
- <sup>36</sup>W. J. Xu, X. Y. Dong, and W. T. Ding, "Analysis of fluid-particle interaction in granular materials using coupled SPH-DEM method," *Powder Technol.* **353**, 459–472 (2019).
- <sup>37</sup>L. Rondon, O. Pouliquen, and P. Aussillous, "Granular collapse in a fluid: Role of the initial volume fraction," *Phys. Fluids* **23**, 073301 (2011).
- <sup>38</sup>A. Bougouin and L. Lacaze, "Granular collapse in a fluid: Different flow regimes for an initially dense-packing," *Phys. Rev. Fluids* **3**, 064305 (2018).
- <sup>39</sup>G. Pinzon and M. Cabrera, "Planar collapse of a submerged granular column," *Phys. Fluids* **31**, 086603 (2019).
- <sup>40</sup>G. Pinzon and M. A. Cabrera, "Submerged planar granular column collapse: Fluid fluxes at the collapsing granular front," in 7th International Conference on Debris-Flow Hazards Mitigation (2018).
- <sup>41</sup>S. F. Wright, I. Zadrzil, and C. Markides, "A review of solid-liquid selection options for optical-based measurements in single-phase liquid, two-phase liquid-liquid and multiphase solid-liquid flows," *Exp. Fluids* **58**, 108 (2017).
- <sup>42</sup>J. A. Dijkstra, F. Rietz, K. A. Lorincz, M. van Hecke, and W. Losert, "Invited article: Refractive index matched scanning of dense granular materials," *Rev. Sci. Instrum.* **83**, 011301 (2012).
- <sup>43</sup>J. Fraczek, A. Zlobecki, and J. Zemanek, "Assessment of angle of repose of granular plant material using computer image analysis," *J. Food Eng.* **83**, 17–22 (2007).
- <sup>44</sup>D. M. Wood, *Soil Behaviour and Critical State Soil Mechanics* (Cambridge University Press, 1991).

- <sup>45</sup>M. Pailha and O. Pouliquen, “A two-phase flow description of the initiation of underwater granular avalanches,” *J. Fluid Mech.* **633**, 115–135 (2009).
- <sup>46</sup>R. M. Iverson, M. Reid, N. R. Iverson, R. LaHusen, M. Logan, J. Mann, and D. Brien, “Acute sensitivity of landslide rates to initial soil porosity,” *Science* **290**, 513–516 (2000).
- <sup>47</sup>A. Armanini, H. Capart, L. Fraccarollo, and M. Larcher, “Rheological stratification in experimental free-surface flows of granular–liquid mixtures,” *J. Fluid Mech.* **532**, 269–319 (2005).
- <sup>48</sup>G. C. Yang, L. Jing, C. Y. Kwok, and Y. D. Sobral, “Pore-scale simulation of immersed granular collapse: Implications to submarine landslides,” *J. Geophys. Res.* **125**, e2019JF005044, <https://doi.org/10.1029/2019JF005044> (2020).
- <sup>49</sup>J. Heyman, “Tractrac: A fast multi-object tracking algorithm for motion estimation,” *Comput. Geosci.* **128**, 11–18 (2019).
- <sup>50</sup>H. Yuen, J. Princen, J. Illingworth, and J. Kittler, “Comparative study of Hough transform methods for circle finding,” *Image Vis. Comput.* **8**, 71–77 (1990).
- <sup>51</sup>W.-T. Zhang, Y. An, Q.-Q. Liu, X.-L. Wang, and Y.-H. Sun, “Evolution of energy in submerged granular column collapse,” *Chin. Phys. Lett.* **37**, 074502 (2020).
- <sup>52</sup>L. Schiller, “A drag coefficient correlation,” *Zeit. Ver. Deutsch. Ing.* **77**, 318–320 (1933).
- <sup>53</sup>P. Jop, Y. Forterre, and O. Pouliquen, “Crucial role of sidewalls in granular surface flows: Consequences for the rheology,” *J. Fluid Mech.* **541**, 167–192 (2005).